







Shahid Chamran
University of Ahvaz

Journal of Applied and Computational Mechanics



Research Paper

Prediction Capabilities of a One-dimensional Wall-flow Particulate Filter Model

Andrea Natale Impiombato¹, Cesare Biserni¹, Massimo Milani², Luca Montorsi²

¹ Department of Industrial Engineering (DIN), School of Engineering and Architecture, Alma Mater Studiorum - University of Bologna,
Viale Risorgimento 2, 40136 Bologna, Italy, Email: andrea.impiombato2@unibo.it, cesare.biserni@unibo.it

² Department of Science and Methods for Engineering, University of Modena and Reggio Emilia,
Viale A. Allegri 9, 42121 Reggio Emilia, Italy: massimo.milani@unimore.it, luca.montorsi@unimore.it

Received September 27 2021; Revised October 14 2021; Accepted for publication October 15 2021.

Corresponding author: A.N. Impiombato (andrea.impiombato2@unibo.it)

© 2022 Published by Shahid Chamran University of Ahvaz

Abstract. This work is focused on the formulation of a numerical model for prediction of flow field inside a particulate filter. More specifically, a one-dimensional mathematical model of the gas flow in a particulate trap-cell is deduced and solved numerically. The results are given in terms of velocity, pressure, and filtration velocity. In addition, the dependence of the pressure drop on the main governing parameters has been investigated. More specifically, the permeability of the porous medium and the hydraulic diameter play a fundamental role in the pressure drop.

Keywords: Particulate filter model; Porous media; Non-dimensional approach; Numerical approach.

1. Introduction

Internal combustion engines, during operation, release quantities of pollutants in aerosol form which are harmful to the environment and human health [1]-[2]. As a consequence, car companies are making use of engine exhaust fume filtering systems to keep pollutant emission levels low [3], while research institutions are exploring the option of developing fully sustainable vehicles (as innovative electric buses [4] or solar powered vehicles to [5,6]). The most common geometry is the wall-flow one, in which the exhaust gases are forced to pass between the filter cells and overcome the porous matrix that separates the different cells (as depicted in Fig. 1). However, inserting the wall-flow filter into the flue gas exhaust duct produces a pressure drop, i.e., the engine must perform more work to overcome it. This affects the performance of the engine, in particular its fuel efficiency. Therefore, the ability to accurately predict the backpressure caused by the filter monolith has become very important for automotive companies in the optimization of their vehicles [7].

Bissett [8] in 1984 proposed a pivotal study regarding the regeneration process of the filter using a one-dimensional numerical resolution approach of the balance equations of mass, moment and energy. This conceptual model constituted the basis for subsequent works aimed at the prediction of the pressure drop under different working conditions of the filter and filtration efficiency. Prantoni et al. [9] adopted the above-mentioned model [8] considering the fluid dynamic interaction between the cells that make up the entire wall-flow filter. Aleksandrova et al. [10] used the Bissett model [8] to characterize particulate filters for diesel engines and for gasoline engines under different flow conditions but at a fixed temperature. Moreover, Koltsakis et al. [11] and Yang et al. [12] recount additional examples of application of Bissett's model [8] for the characterization of particulate filters. The majority of these models, such as the one here developed, are based on a scaling approach so that the pressure drop of the filter can be modelled by considering a simplified geometry including a single inlet and outlet channel. In coherence with Prantoni et al. [9], the approximation introduced by the scaling approach can be justified when the velocity profile entering the filter is flat, so that the mass flow rate is the same in all channels, and when the ratio between the cell hydraulic diameter and the filter diameter is very small ($d/D_{filter} \ll 1$). In other words, it means that the full coupling between open and closed channels is negligible on the scale of the entire filter. It is worth mentioning that the applicability of the scaling approach is also limited to filters with homogeneous properties, i.e. all the cells have the same hydraulic diameter, all the porous walls have the same permeability, and soot is distributed homogeneously.

The efficiency of the filter varies over time according to the augmentation of the soot thickness. The simulation of this scenario requires the modelling of the interaction events between particles and porous matrix (Lattice-Boltzmann method), with high computational cost (see [13]-[15]). Another problem that affects the simulation of a real porous medium is the modelling of geometry. On this regard, some authors used the Voronoi tessellation (as reported in [16], [17]), while others used real images obtained from an X-ray analysis [18]. Both these approaches proved to be unreliable for solving equations of motion, especially when analyzing large systems. The unsurpassed approach is still to model the porous medium through the Darcy equation, in coherence with Celli et al. [19], and Tilton et al. [20], as will be described in next Paragraph 2.



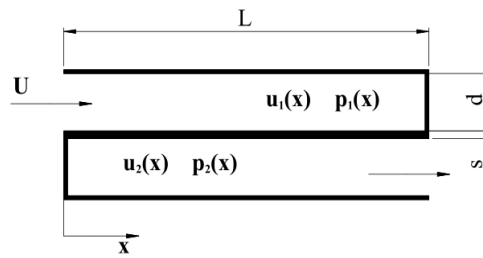


Fig. 1. Wall-flow Particulate filter: single trap cell model where U is the inlet cell velocity, L is the monolith length, d is the cell dimension equal to the hydraulic diameter, s is the porous wall thicknesses, $u_1(x)$ is the velocity field in the inlet cell, $u_2(x)$ is the velocity field in the outlet cell, $p_1(x)$ is the pressure field in the inlet cell and $p_2(x)$ is the pressure field in the outlet cell.

The major application that the system under consideration is applied is the automotive sector. In general an automotive is a quite complex electro-mechanical system consisting of a large number of subsystems and components. Dealing with systems of such a complexity implies a versatile research approach ranging from modeling tasks [21, 22], over optimization of various components [23, 24], engines [25, 26], to aspects of computational fluid dynamics [27, 28], etc. However, all filter systems have an impact on other aspects as well, such as noise, vibrations [29].

The present work deals with a one-dimensional mathematical model of the particulate wall-flow filter in stationary conditions and with the hypothesis of constant temperature system. In particular, the model is developed considering the pressure dependent gas density through the ideal gas law. The model is non-dimensionalized and the results are validated by comparison with the literature [30]. Furthermore, a sensitivity analysis has been carried out by correlating the pressure drop of the gas flow through the filter with the variation of the system parameters (hydraulic diameter (d), porous media wall thicknesses (s), monolith length (L), permeability porous media (k) and dynamic viscosity (μ)). The model is solved numerically in MATLAB ambient [31].

2. Physical Domain and Mathematical Model

In Fig. 1, the configuration of the Wall-Flow filter used in this work is depicted: the flow inside a honeycomb cell is considered. The gas flow is forced to enter the inlet cell (cell 1), cross the porous medium and finally to pass in the outlet cell (cell 2), communicating with the environment after the filter. In coherence with Konstandopoulos et al [32], the one-dimensional mass (Eq. (1)) and momentum (Eq. (2)) balance equations of the exhaust gas can be defined for the inlet cell (subscript 1) and outlet cell (subscript 2):

$$\frac{d}{dx}(\rho_1 u_1) = -\frac{4}{d} \rho_1 v_f, \tag{1}$$

$$\frac{d}{dx}(\rho_2 u_2) = \frac{4}{d} \rho_2 v_f, \tag{2}$$

$$\frac{d}{dx}(\rho_1 u_1^2) = -\frac{dp_1}{dx} - 2 f Re \frac{\mu}{d^2} u_1, \tag{3}$$

$$\frac{d}{dx}(\rho_2 u_2^2) = -\frac{dp_2}{dx} - 2 f Re \frac{\mu}{d^2} u_2, \tag{4}$$

where ρ is the fluid density, u is the fluid velocity, d is the hydraulic cell diameter, v_f is the filtration velocity trough the porous wall, p is the pressure, μ is the fluid dynamic viscosity, f is the friction factor and Re is the Reynolds number.

The filtration velocity v_f is related to Darcy's law:

$$p_1 - p_2 = \frac{\mu}{k} s v_f, \tag{5}$$

where k is the porous medium permeability and s is the porous medium thickness.

The boundary conditions are expressed as follows:

$$u_1(0) = U, \tag{6}$$

$$u_1(L) = 0, \tag{7}$$

$$u_2(0) = 0, \tag{8}$$

$$p_2(L) = p_{atm}, \tag{9}$$

where L is the monolith length, U is the inlet cell velocity and p_{atm} is the pressure at the outlet cell imposed equal to atmospheric pressure.

Eqs. (6)-(7) indicate that the inlet cell velocity is known at the entrance and at the termination, Eq. (8) expresses the impermeability of the outlet cell at $x=0$, and Eq. (9) states that the exhaust gas is exiting at a known atmospheric pressure.



Substituting the filtration velocity v_f (formulated in Eq. (5)) into Eqs. (1)-(2), we obtain:

$$\frac{d}{dx}(\rho_1 u_1) = -\frac{4}{d} \rho_1 \frac{k}{\mu S} (p_1 - p_2), \tag{10}$$

$$\frac{d}{dx}(\rho_2 u_2) = -\frac{4}{d} \rho_2 \frac{k}{\mu S} (p_1 - p_2). \tag{11}$$

According to the ideal gas law [33], the local density can be defined as a function of the pressure p_i :

$$\rho_i = \frac{p_i}{RT}, \quad i = 1, 2 \tag{12}$$

where R is the air specific gas constant equal to 287.058 J/(kg K) and T is the temperature.

By substituting Eq. (12) into Eqs. (10)-(11) and Eqs. (3)-(4), the following differential set of equations is obtained:

$$\frac{d}{dx}(p_1 u_1) = -\frac{4}{d} \frac{k}{\mu S} p_1 (p_1 - p_2), \tag{13}$$

$$\frac{d}{dx}(p_2 u_2) = \frac{4}{d} \frac{k}{\mu S} p_2 (p_1 - p_2), \tag{14}$$

$$\frac{1}{RT} \frac{d}{dx}(p_1 u_1^2) = -\frac{dp_1}{dx} - 2 f Re \frac{\mu}{d^2} u_1, \tag{15}$$

$$\frac{1}{RT} \frac{d}{dx}(p_2 u_2^2) = -\frac{dp_2}{dx} - 2 f Re \frac{\mu}{d^2} u_2. \tag{16}$$

Eqs. (13)-(16) coupled with the boundary conditions Eqs. (6)-(9) represent the Boundary Value Problem (BVP) whose unknowns variables are $u_i(x)$ and $p_i(x)$ with $i=1,2$.

Introducing L as a length scale, U as the axial velocity scale, and $dU/4L$ as the transverse (wall) velocity scale, the governing equation can be expressed in terms of the following dimensionless quantities:

$$\bar{x} = \frac{x}{L}, \quad \bar{u}_i = \frac{u_i}{U} \quad (i = 1, 2), \quad \bar{p}_i = \frac{p_i - p_{atm}}{p} \quad (i = 1, 2), \quad p^* = \frac{\mu U d S}{4 L k}. \tag{17}$$

Finally, the dimensionless equations and boundary conditions are given by:

$$\frac{d}{d\bar{x}}(\bar{p}_1 \bar{u}_1) + a \frac{d\bar{u}_1}{d\bar{x}} = -(\bar{p}_1 + a)(\bar{p}_1 - \bar{p}_2), \tag{18}$$

$$\frac{d}{d\bar{x}}(\bar{p}_2 \bar{u}_2) + a \frac{d\bar{u}_2}{d\bar{x}} = (\bar{p}_2 + a)(\bar{p}_1 - \bar{p}_2), \tag{19}$$

$$\frac{d}{d\bar{x}}(\bar{p}_1 \bar{u}_1^2) + a \frac{d\bar{u}_1^2}{d\bar{x}} = -b \frac{d\bar{p}_1}{d\bar{x}} - a b c \bar{u}_1, \tag{20}$$

$$\frac{d}{d\bar{x}}(\bar{p}_2 \bar{u}_2^2) + a \frac{d\bar{u}_2^2}{d\bar{x}} = -b \frac{d\bar{p}_2}{d\bar{x}} - a b c \bar{u}_2, \tag{21}$$

$$\bar{u}_1(0) = 1, \tag{22}$$

$$\bar{u}_1(1) = 0, \tag{23}$$

$$\bar{u}_2(0) = 0, \tag{24}$$

$$\bar{p}_2(1) = 0, \tag{25}$$

where a , b and c are parameters defined as:

$$a = \frac{P_{atm}}{P}, \quad b = \frac{RT}{U^2}, \quad c = 2 f Re \frac{\mu}{d^2} \frac{LU}{p_{atm}}. \tag{26}$$

For the sake of conciseness, the complete non-dimensional procedure of equations has been reported in Appendix A.

In this study, a sensitivity analysis of the boundary value problem Eqs. (18)-(25) has been pointed out by varying the parameters a , b and c in accordance with the real physics conditions defined in Table 1.



Table 1. Parameters set up [12].

Name	Symbol	Value	Units
Hydraulic diameter	d	0.001	m
Porous wall thicknesses	s	0.0002	m
Monolith length	L	0.125	m
Permeability porous media	k	5.5×10^{-13}	m^2
Gas constant	R	287.05	$J/(kg K)$
Temperature	T	700	K
Atmospheric pressure	p_{atm}	101325	Pa

More specifically, the analysis was conducted by varying one physical property at a time, maintaining the other constants at the values indicated in Table 1.

The variation of dynamic viscosity with temperature T has been calculated using the Sutherland's Law [34]:

$$\mu(T) = \mu_{ref} \left(\frac{T}{T_{ref}} \right)^{3/2} \frac{T_{ref} + S}{T + S}, \tag{27}$$

$$T_{ref} = 273,15K, \mu_{ref} = 1,76 \cdot 10^{-5} \frac{kg}{ms}, S = 110,4K.$$

The product between the friction factor f and Reynold's number Re was obtained following the fully developed square tube theory [35] so that $f Re = 14,227$. Thus, the starting calculated values of the parameters are $a=209.076$, $b=502.338$ and $c=0.0234$.

3. Numerical Procedure and Model Validation

The non-dimensional Boundary Value Problem (Eqs. (18)-(25)) was solved numerically in MATLAB ambient[31], by means of the "bvp4c" solver, a finite difference code that implements the four-stage Lobatto IIIa formula [36]. The latter is a collocation formula providing a C1-continuous solution that is fourth-order accurate uniformly in the interval of integration. Mesh selection and error control are based on the residual of the continuous solution. The collocation technique uses a mesh of points to divide the interval of integration into subintervals. The solver determines a numerical solution by resolving a global system of algebraic equations resulting from the boundary conditions, and the collocation conditions imposed on all the subintervals. More specifically, the computed solution $S(x)$ is the exact solution of a perturbed problem $S'(x) = f(x,S(x)) + res(x)$. On each subinterval of the mesh, a norm of the residual in the i -th component of the solution, $res(i)$, is estimated and has not to exceed an imposed tolerance. This tolerance is a function of the relative and absolute tolerances, here fixed equal to $RelTol=10^{-5}$, and $AbsTol=10^{-6}$.

$$\left(\frac{res(i)}{\max \left(|f(i)|, \frac{|AbsTol(i)|}{RelTol} \right)} \right) \leq RelTol. \tag{28}$$

Therefore, if the solution does not satisfy the tolerance criteria, the solver adapts the mesh and repeats the process. What is needed is to provide the initial mesh points, as well as an initial approximation of the solution in the mesh points. Regarding the case here treated, the domain $[0,1]$ has been divided into 100 points.

Therefore, in order to validate the model described in Section 2 (Eqs. (18)-(27)), the velocity fields inside the single cells have been compared with the results obtained by J.D. Cooper et al. [30]. In turn, the solution illustrated in Ref. [30] had been validated by means of experimental results taken from a magnetic resonance imaging (MRI), considering a trap-cell with the following characteristics: (i) monolith length $L= 0,145 m$, (ii) hydraulic diameter $d=0.001 m$, (iii) porous wall thickness $s=0.0002 m$, (iv) permeability porous media $k=5.5 \times 10^{-13} m^2$, (v) temperature 295 K.

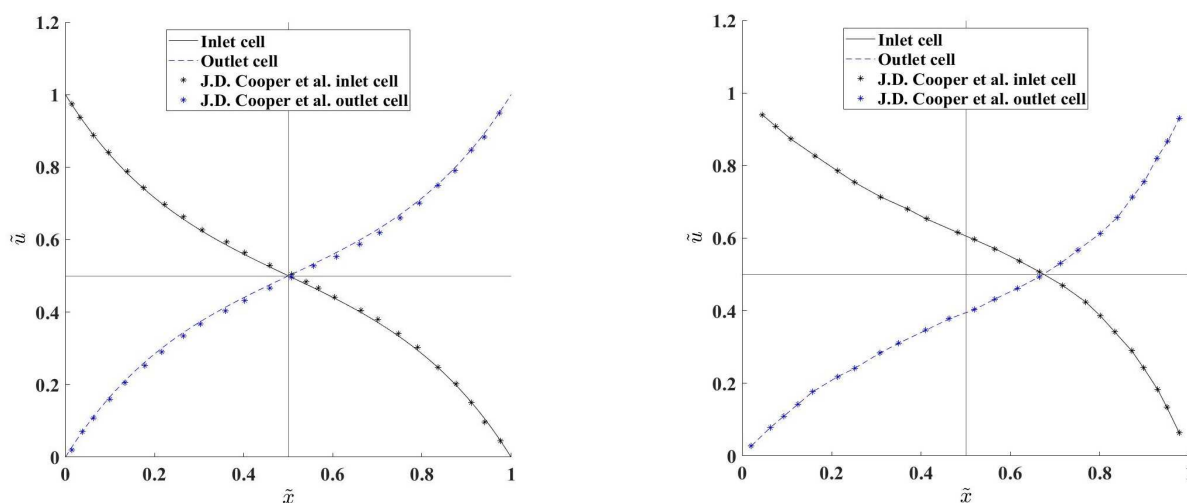


Fig. 2. Comparison between non-dimensional velocity profiles (here found and the ones obtained by J.D. Cooper et al. [30]) with reference to the inlet cell (black line and black points) and outlet cell (blue dashed line and blue points), for two values of velocity inlet: (left) 0.044 m/s and (right) 0.525 m/s.



Table 2. Numerical values of the comparison illustrated in Fig. 2 and percentual error.

\bar{x}	Home Code		J.D. Cooper		$\epsilon\%$		Home Code		J.D. Cooper		$\epsilon\%$	
	Inlet	Outlet	Inlet	Outlet	Inlet	Outlet	Inlet	Outlet	Inlet	Outlet	Inlet	Outlet
0	1	0	1	0	0	0	1	0	1	0	0	0
0.25	0.6756	0.3244	0.6759	0.3235	0.044	0.280	0.7548	0.048	0.7563	0.050	0.200	4.170
0.5	0.5013	0.4967	0.5012	0.5028	0.020	1.230	0.6051	0.026	0.6091	0.024	0.660	7.690
0.75	0.3339	0.6661	0.3342	0.6723	0.090	0.930	0.4427	0.089	0.4483	0.090	1.260	1.120
1	0	1	0	1	0	0	0	1	0	1	0	0

Figure 2 highlights the comparison between the velocity profiles in both inlet and outlet cells. Based on pure observation, there are no major discrepancies between the solutions, as confirmed by the error value ϵ reported in Table 2 that was computed according to the following equation:

$$\epsilon = \frac{|\bar{v}_i - \bar{v}_{ref}|}{\bar{v}_i} \tag{29}$$

where \bar{v}_i is the value obtained using the home code and \bar{v}_{ref} is the value taken from Ref. [30].

4. Results and Discussion

In the following sections, the velocity and pressure fields in the two cells are analyzed as the governing parameters of the problem vary.

4.1 Influence of Hydraulic Diameter

Figure 3 shows the behavior of the non-dimensional velocity \bar{u} in the inlet and outlet cells for different values of the hydraulic diameter d ($d=0.5$ mm, $d=1$ mm and $d=2$ mm), and for fixed values of the inlet velocity U ($U=1$ m/s and $U=50$ m/s).

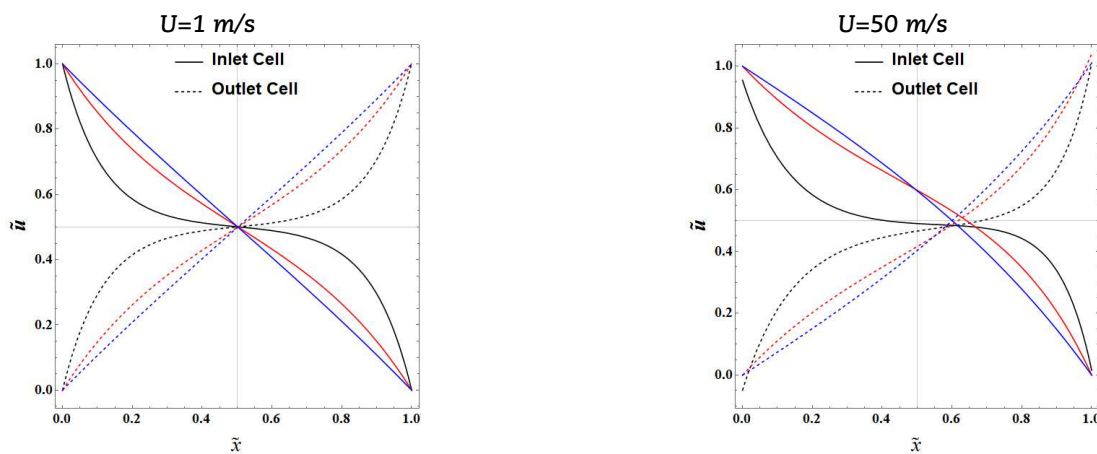


Fig. 3. Non-dimensional velocity \bar{u} in the inlet (continues line) and outlet (dashed line) cell along the non-dimensional coordinate \bar{x} as a function of the inlet velocity U and the hydraulic diameter d : $d=0.5$ mm (black lines), $d=1$ mm (red lines) and $d=2$ mm (blue lines).

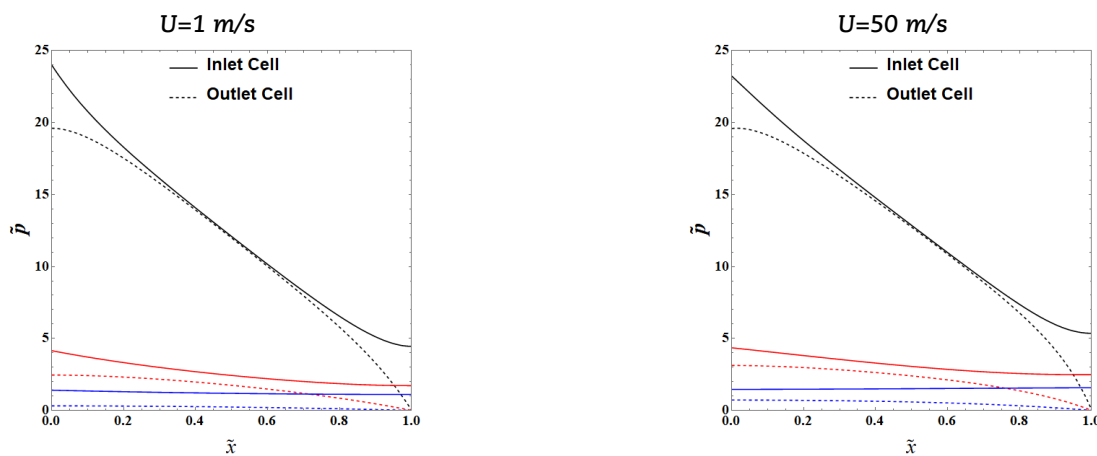


Fig. 4. Non-dimensional pressure \bar{p} in the inlet (continues line) and outlet (dashed line) cell along the non-dimensional coordinate \bar{x} as a function of the inlet velocity U and the hydraulic diameter d : $d=0.5$ mm (black lines), $d=1$ mm (red lines) and $d=2$ mm (blue lines).



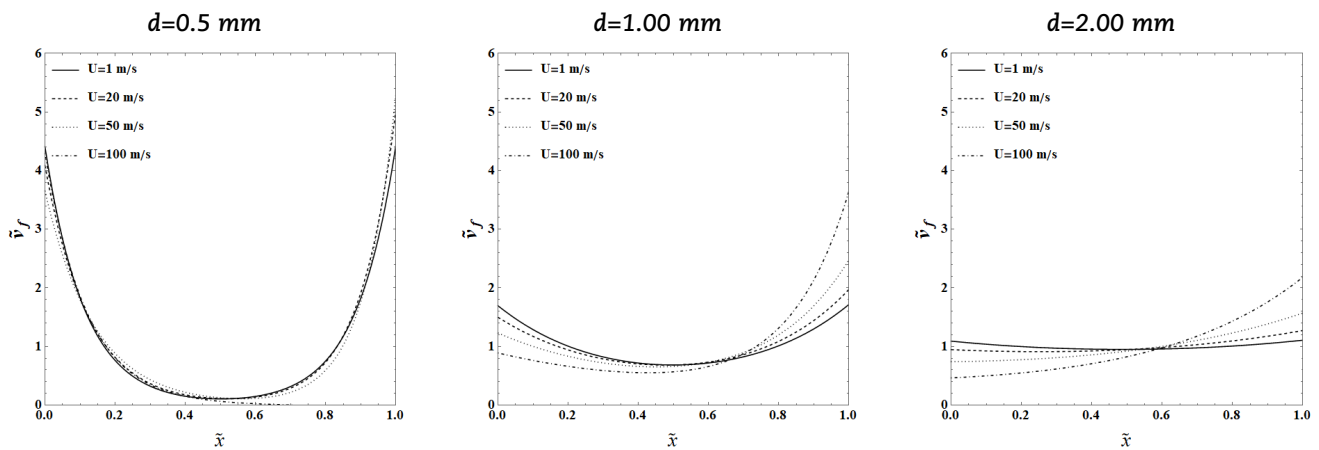


Fig. 5. Non-dimensional filtration velocity \tilde{v}_f in the inlet/outlet cell along the non-dimensional coordinate \tilde{x} , as a function of hydraulic diameter d and of the inlet velocity U .

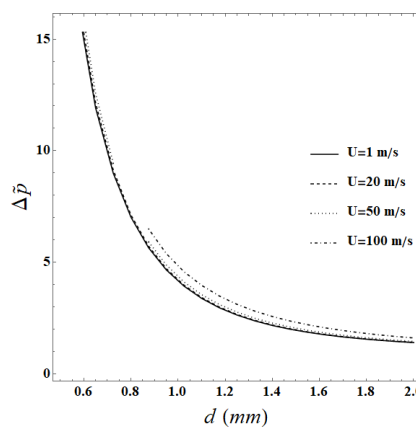


Fig. 6. Non-dimensional pressure drop $\Delta\tilde{p}$ as a function of the hydraulic diameter d and the inlet velocity U .

Based on pure observation, the behavior of the non-dimensional velocity \tilde{u} inside the cells (inlet and outlet) is symmetrical. More specifically, as the velocity U increases, the intersection point between the two velocity functions tends to move towards the exit ($0.5 < \tilde{x} < 1$). Please also note that as the hydraulic diameter increases the two velocity functions approximate a linear profile, especially for low values of the inlet velocity U .

Figure 4 highlights the influence of the pressure drop. More specifically, Fig. 4 shows the non-dimensional pressure \tilde{p} trend inside the inlet and outlet cells for different values of the hydraulic diameter d ($d=0.5\text{ mm}$, $d=1\text{ mm}$ and $d=2\text{ mm}$) at the same fixed values of the inlet velocity U ($U=1\text{ m/s}$ and $U=50\text{ m/s}$). The shape of the non-dimensional pressure \tilde{p} profile is more influenced by the value of the hydraulic diameter d . For low values of d , significant pressure gaps between the start and end of each cell are detected. The opposite happens for higher values of the hydraulic diameter in which the pressure differences between start and end of the cell decrease.

Moreover, the pressure trend regulates, according to Darcy's law Eq. (5), the filtration velocity \tilde{v}_f . On this regard, Fig. 5 shows the non-dimensional filtration velocity trend (see Appendix B for non-dimensionalizing procedure) as a function of the hydraulic diameter d and for different values of the velocity inlet U . It is important to underline that the curves corresponding to velocity $U = 100\text{ m/s}$ are purely numerical as these velocity value is not real.

The filtration velocity proves to be highly influenced by the hydraulic diameter d , being in turn the pressure difference between the two cells highly affected by the value of this parameter.

It is worth mentioning that the total pressure drop between the entrance and the exit of the trap-cell is of great importance in engineering:

$$\Delta\tilde{p} = \tilde{p}_1(0) - \tilde{p}_2(1). \tag{30}$$

With reference to the model here developed, $\tilde{p}_2(1)$ is equal to 0, due to the imposed boundary condition (see Eq. (25)), so that Eq. (30) is reduced to the value $\tilde{p}_1(0)$.

Finally, Fig. 6 shows the pressure drop $\Delta\tilde{p}$ as a function of the hydraulic diameter d evaluated for different value of the velocity U . The pressure drop $\Delta\tilde{p}$ is a decreasing monotone function of the hydraulic diameter d , while the velocity U has slight influence.

4.2 Influence of Porous Wall Thickness

The behavior of the thickness porous media s (Figs. 7-10) is similar to that of hydraulic diameter previously analyzed. The non-dimensional velocity shape \tilde{u} in the two cells tends towards linearity with the augmentation of the thickness porous media s (Fig. 7). The increase of the velocity U , on the other hand, tends to shift the crossing point between the velocity functions by values \tilde{x} exceeding 0.5. The velocity distribution \tilde{p} is regulated by the non-dimensional pressure \tilde{p} , as depicted in Fig. 8.



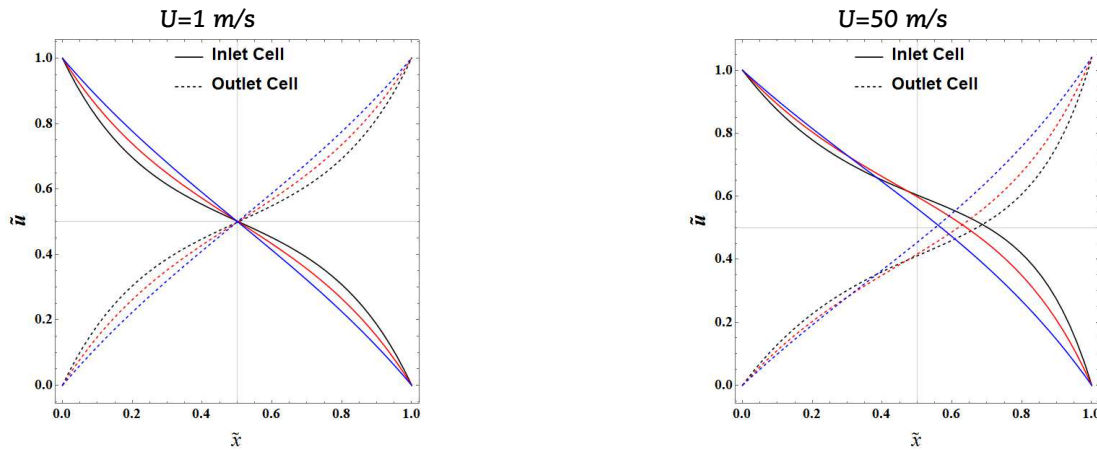


Fig. 7. Non-dimensional velocity \tilde{u} in the inlet (continues line) and outlet (dashed line) cell along the non-dimensional coordinate \tilde{x} as a function of the inlet velocity U and the thickness porous media s : $s=0.1$ mm (black lines), $s=0.2$ mm (red lines) and $s=0.6$ mm (blue lines).

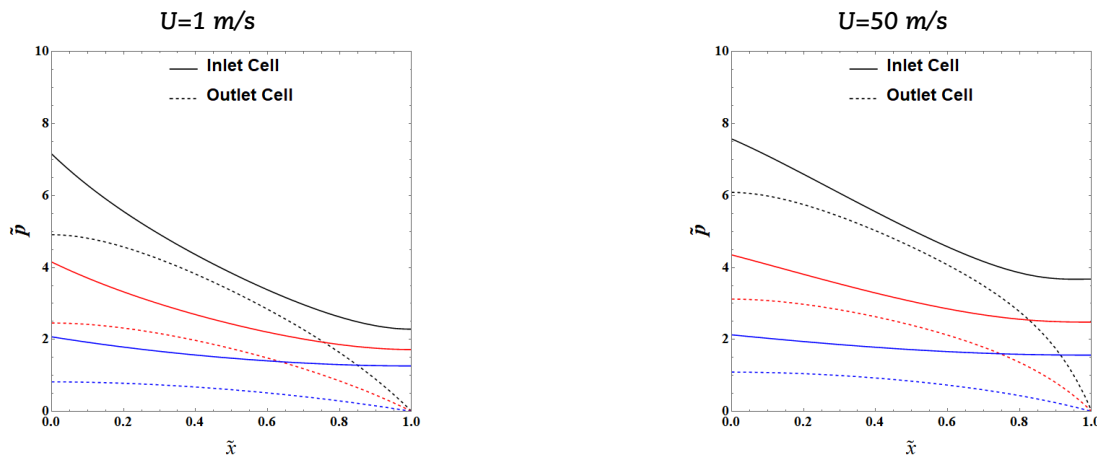


Fig. 8. Non-dimensional pressure \tilde{p} in the inlet (continues line) and outlet (dashed line) cell along the non-dimensional coordinate \tilde{x} as a function of the inlet velocity U and the thickness porous media s : $s=0.1$ mm (black lines), $s=0.2$ mm (red lines) and $s=0.6$ mm (blue lines).

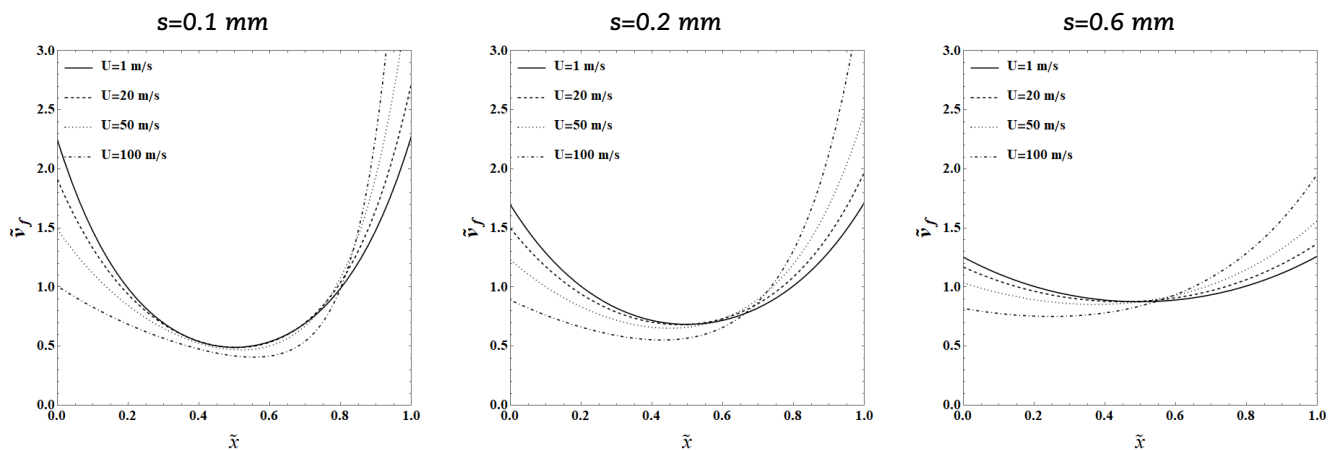


Fig. 9. Non-dimensional filtration velocity \tilde{v}_f in the inlet/outlet cell along the non-dimensional coordinate \tilde{x} as a function of the thickness porous media s and Inlet velocity U .

It is visible that the thickness of the porous medium s causes the pressure distribution to vary more significantly than due to the velocity U . This pressure distribution, through Darcy's law, also regulates the filtration velocity \tilde{v}_f (Fig. 9), which in turn indicates the depths of the filter. It is important to underline that the curves corresponding to velocity $U = 100$ m/s are purely numerical as these velocity value is not real.

In addition, Fig. 10 shows that the pressure drop $\Delta\tilde{p}$ (eq. (28)) decreases monotonically with the augmentation of the thickness of porous media. The simulations are carried out by holding constant all the other parameters. In particular, the total permeability of the porous media is the same while increasing its thickness. This is affecting the pressure drop along the cell length and determines a more uniform pressure distribution.



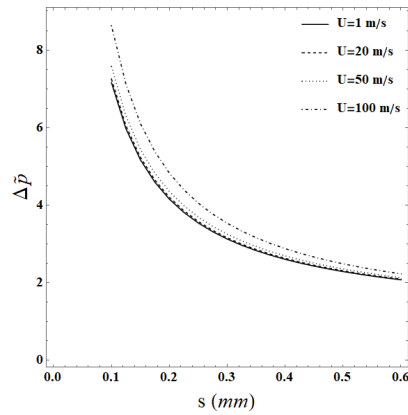


Fig. 10. Non-dimensional pressure drop $\Delta\bar{p}$ as a function of the thickness porous media s and Inlet velocity U .

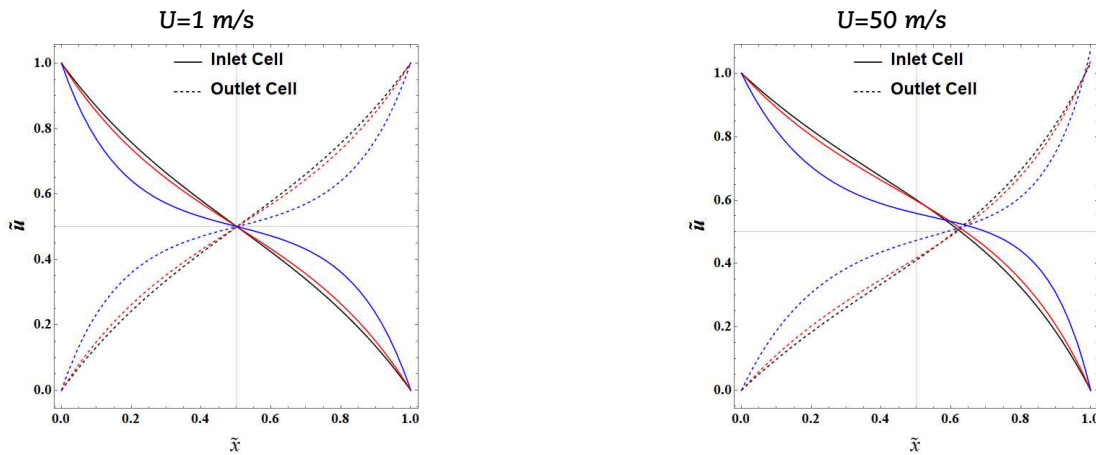


Fig. 11. Non-dimensional velocity \bar{u} in the inlet (continues line) and outlet (dashed line) cell along the non-dimensional coordinate \bar{x} as a function of the inlet velocity U and the monolith length L : $L=100\text{ mm}$ (black lines), $L=125\text{ mm}$ (red lines) and $L=250\text{ mm}$ (blue lines).

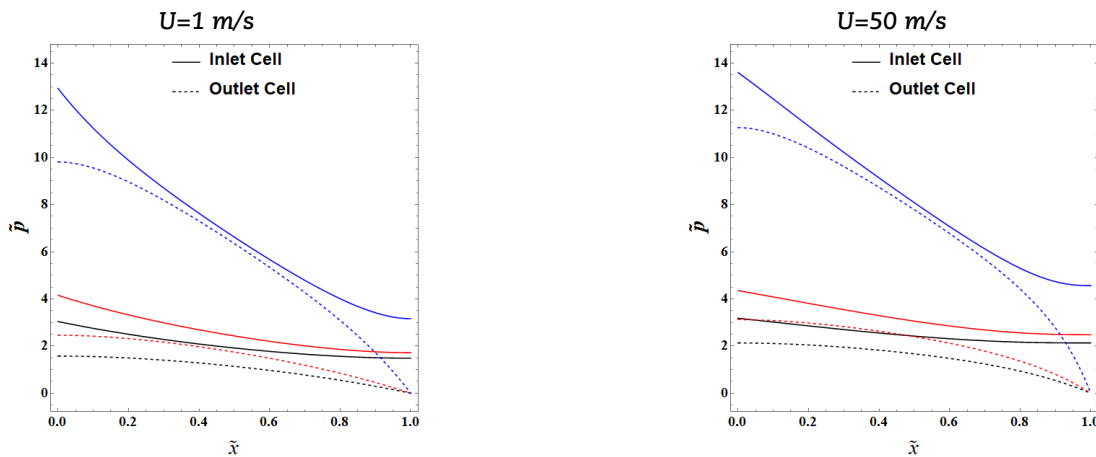


Fig. 12. Non-dimensional pressure \bar{p} in the inlet (continues line) and outlet (dashed line) cell along the non-dimensional coordinate \bar{x} as a function of the inlet velocity U and the monolith length L : $L=100\text{ mm}$ (black lines), $L=125\text{ mm}$ (red lines) and $L=250\text{ mm}$ (blue lines).

4.3 Influence of Monolith Length

The influence of the monolith length L is reported graphically in Figs. 11-14. This parameter presents an opposite behavior if compared to the previous cases. As the value of the monolith length L increases, the velocity profiles deviate from linearity (see Fig. 11). While, as the inlet cell velocity U increases, the intersection point between the curves moves to the $\bar{x} > 0.5$ domain area.

In addition, the pressure \bar{p} trend increases its gradient with the augmentation of the monolith length L , as depicted in Fig. 12. The pressure \bar{p} trend between the two cells also regulates the filtration velocity \bar{v}_f ; on this regard, Fig. 13 demonstrates that it takes a parabolic shape that becomes more pronounced as L increases. It is important to underline that the curves corresponding to velocity $U = 100\text{ m/s}$ are purely numerical as these velocity value is not real. This means that the most “filtering parts” of the filter are those at the extremes. Finally, the pressure drop $\Delta\bar{p}$ increases with the augmentation of the monolith length L , as depicted in Fig. 14.



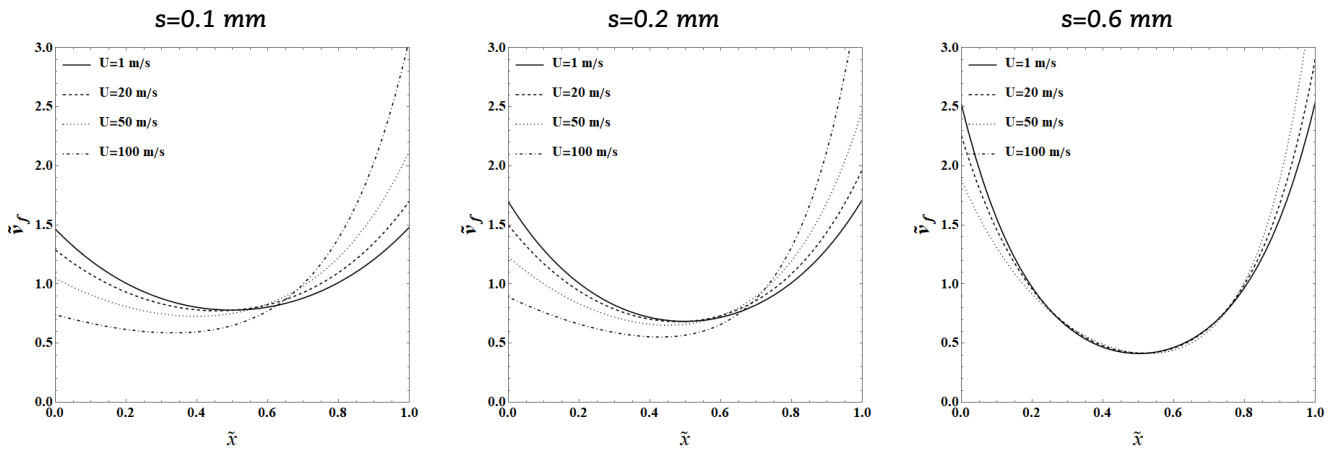


Fig. 13. Non-dimensional filtration velocity \bar{v}_f in the inlet/outlet cell along the non-dimensional coordinate \bar{x} as a function of the monolith length L and inlet velocity U .

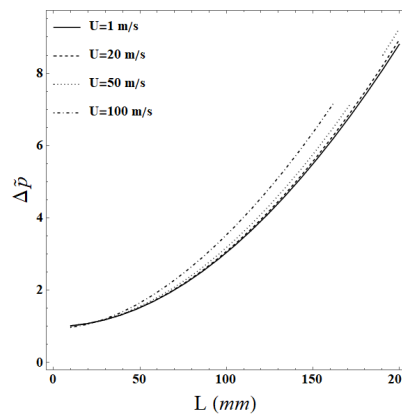


Fig. 14. Non-dimensional pressure drop $\Delta\bar{p}$ as a function of the monolith length L and the inlet velocity U .

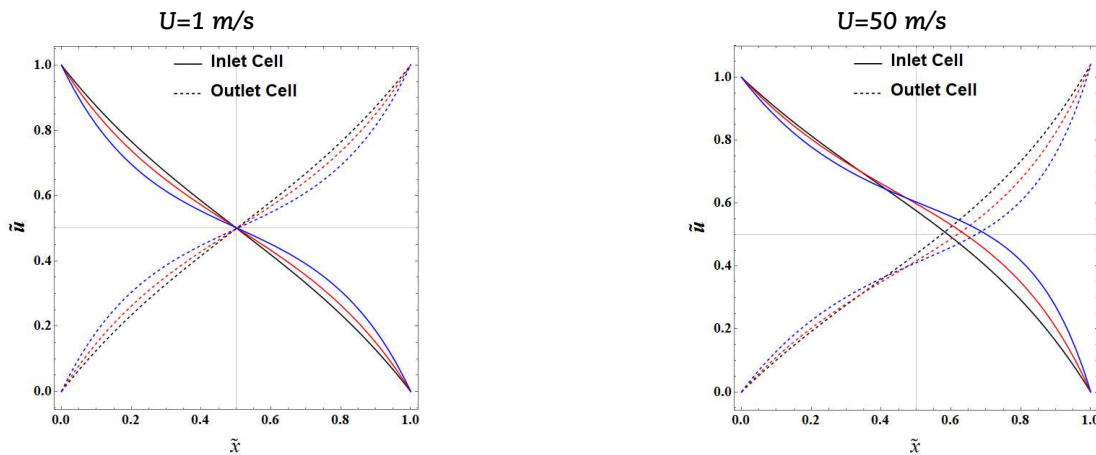


Fig. 15. Non-dimensional velocity \bar{u} in the inlet (continues line) and outlet (dashed line) cell along the non-dimensional coordinate \bar{x} as a function of the inlet velocity U and the permeability porous media k : $k=2.75 \times 10^{-13} \text{ m}^2$ (black lines), $k=5.50 \times 10^{-13} \text{ m}^2$ (red lines) and $k=11.00 \times 10^{-13} \text{ m}^2$ (blue lines).

4.4 Influence of Porous Media Permeability

As can be observed from Fig. 15 and Fig. 16, no major differences are detected in the velocity and pressure fields as the permeability of porous media varies. The increase in the inlet velocity U shifts the intersection between the velocity profiles in the part of the domain with $\bar{x} > 0.5$, while the pressure field increases slightly by module.

This observation is confirmed in Fig. 17, in which it is also noted that the filtration velocity remains approximately the same. The variation of the porous medium permeability k has a linear effect on the pressure drop $\Delta\bar{p}$. As shown in Fig. 18, as the permeability k increases, the pressure drop $\Delta\bar{p}$ increases monotonically and its slope depends on the incoming velocity value. It is important to underline that the curves corresponding to velocity $U = 100 \text{ m/s}$ are purely numerical as these velocity value is not real.



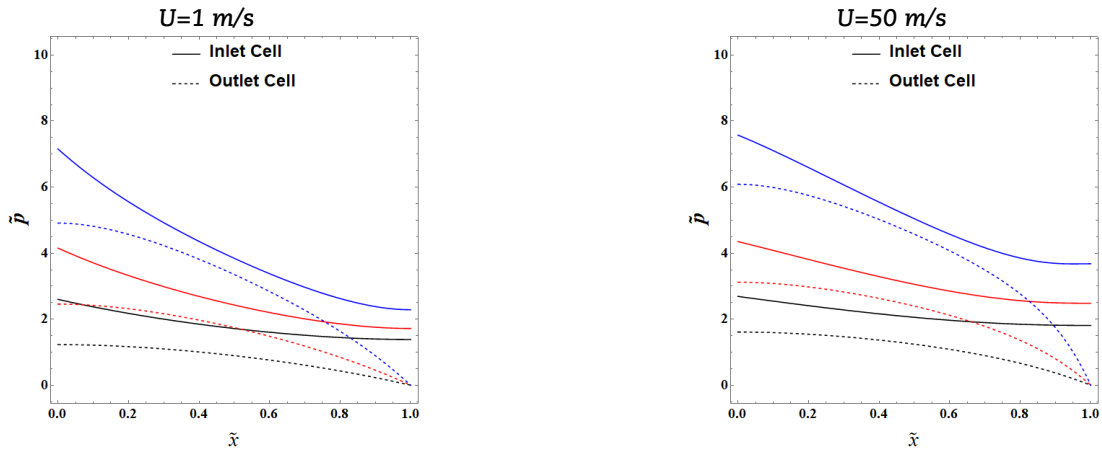


Fig. 16. Non-dimensional pressure \tilde{p} in the inlet (continues line) and outlet (dashed line) cell along the non-dimensional coordinate \tilde{x} as a function of the inlet velocity U and the permeability porous media k : $k=2.75 \times 10^{-13} \text{ m}^2$ (black lines), $k=5.50 \times 10^{-13} \text{ m}^2$ (red lines) and $k=11.00 \times 10^{-13} \text{ m}^2$ (blue lines).

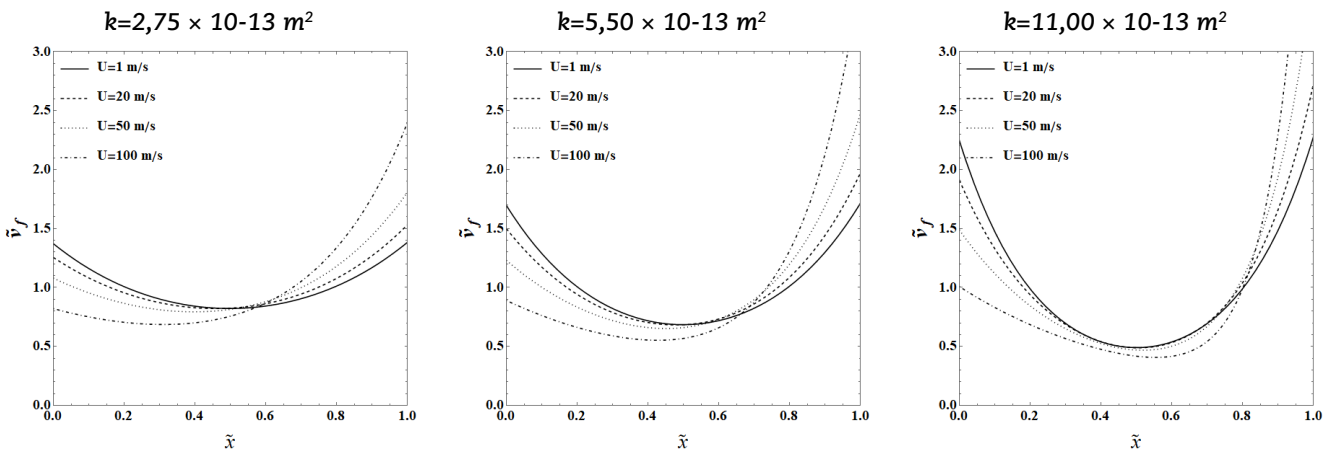


Fig. 17. Non-dimensional filtration velocity \tilde{v}_f in the inlet/outlet cell along the non-dimensional coordinate \tilde{x} as a function of the permeability porous media k and the inlet velocity U .

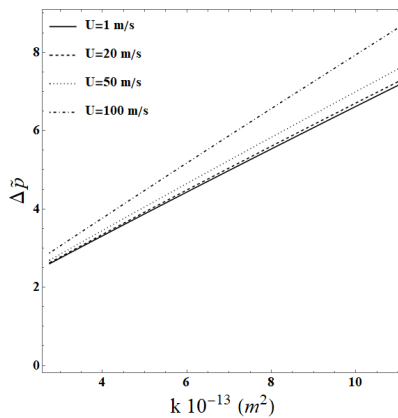


Fig. 18. Non-dimensional pressure drop $\Delta \tilde{p}$ as a function of the permeability porous media k and inlet velocity U .

4.5 Influence of Dynamic Viscosity

The influence of the dynamic viscosity μ has been investigated taking into account the temperature T of the system, according to eq. (27). For sake of clarity, Fig. 19 represents graphically eq. (27) as a function of temperature, within the considered range [400 K, 1000 K]. Based on pure observation, the gas viscosity increases with the augmentation of temperature, due to the forces generated by the molecular collision [37]. As shown in Figs. 20 and 21, the behavior of velocity and pressure fields is mainly affected by the variation of the velocity entering in the first cell.



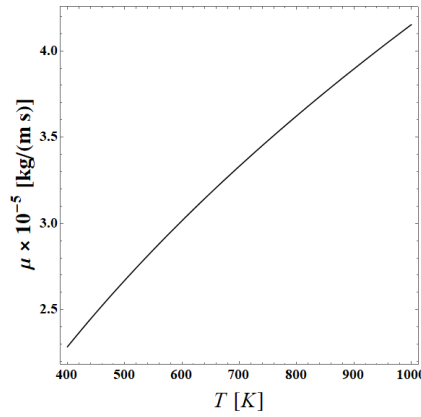


Fig. 19. Dynamic viscosity as a function of temperature according to the Sutherland's Law (Eq. (27)).

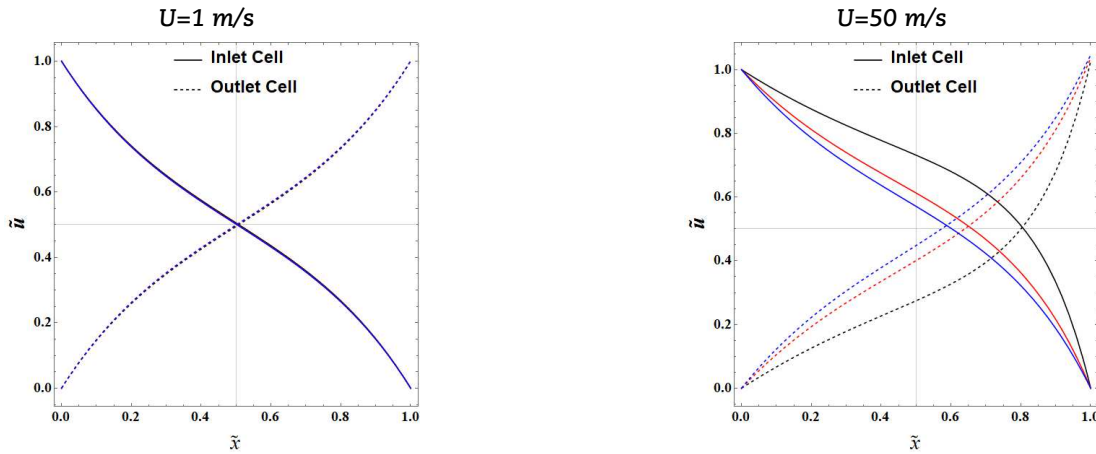


Fig. 20. Non-dimensional velocity \tilde{u} in the inlet (continues line) and outlet (dashed line) cell along the non-dimensional coordinate \tilde{x} as a function of the inlet velocity U and the viscosity μ in function of different temperature T values: $T=400$ K (black lines), $T=700$ K (red lines) and $T=1000$ K (blue lines).

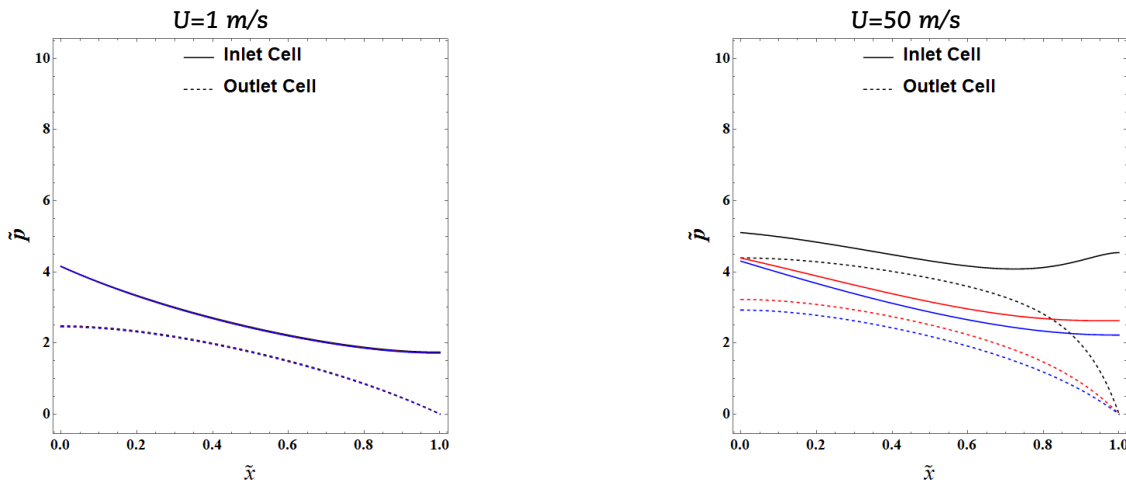


Fig. 21. Non-dimensional pressure \tilde{p} in the inlet (continues line) and outlet (dashed line) cell along the non-dimensional coordinate \tilde{x} as a function of the inlet velocity U and the viscosity μ in function of different temperature T values: $T=400$ K (black lines), $T=700$ K (red lines) and $T=1000$ K (blue lines).

Figure 22 corroborates that the dynamic viscosity μ has the same trend influence on the velocity filtration. It is important to underline that the curves corresponding to velocity $U = 100$ m/s are purely numerical as these velocity value is not real.

Furthermore, Fig. 23 shows that the pressure drop $\Delta\tilde{p}$ is more affected by the inlet cell velocity U than by the system temperature T .



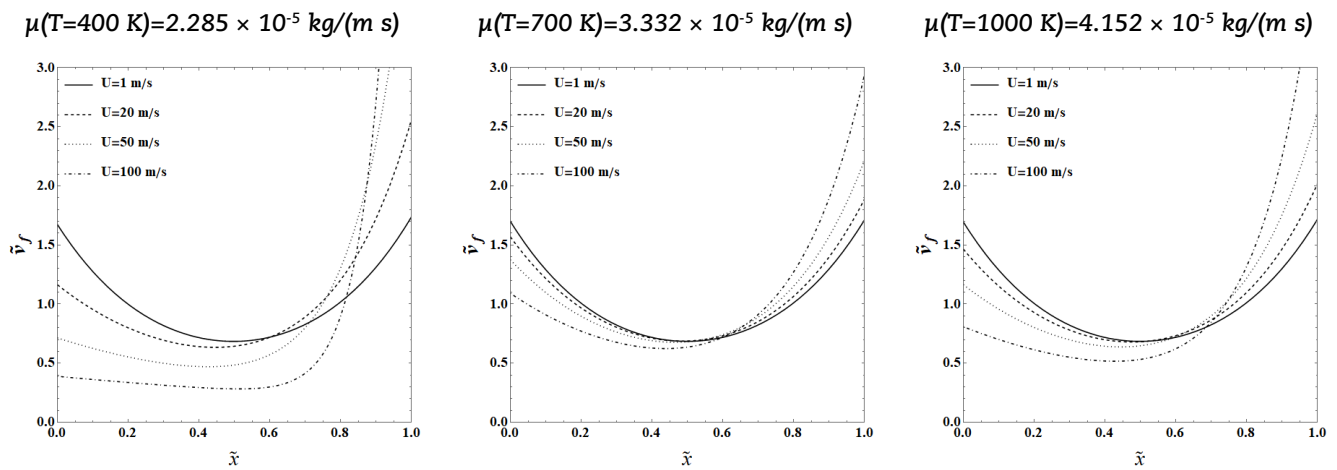


Fig. 22. Non-dimensional filtration velocity \tilde{v}_f in the inlet/outlet cell along the non-dimensional coordinate \tilde{x} as a function of Inlet velocity U and the viscosity μ in function of different temperature T .

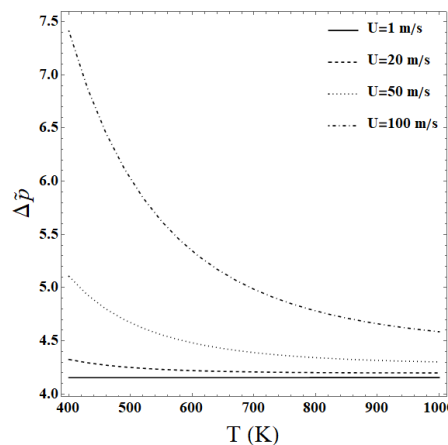


Fig. 23. Non-dimensional pressure drop $\Delta\tilde{p}$ as a function of inlet velocity U and the viscosity μ in function of different temperature T .

5. Conclusion

In this work a one-dimensional model of the elementary cell of the honeycomb particulate filter has been defined. In particular, a sensitivity analysis of a wall-flow filter was carried out. The non-dimensional mass and moment balance equations were solved numerically by modelling the filtration process through the porous layer according to Darcy’s law. The model was validated against experimental work available in literature.

Several conclusions and ideas for future research emerged from this study. The results show how the variation of the governing parameters affects the system fluid dynamics so that the filter generates a different pressure drop. The pressure drop has trends that depend on the velocity value entering the cell. In general, at a fixed gas inlet velocity, a decrease of pressure drop occurs as the (i) hydraulic diameter increases, (ii) the thickness of the porous medium that separates the different cells increases and (iii) the viscosity of the gas increases. Instead, the pressure drop undergoes an increasing trend as (iv) the monolith length increases and (v) the porous medium permeability increases.

More specifically, the permeability of the porous medium plays a fundamental role in the pressure drop: since, as it increases, the pressure drop values increase by an order of magnitude. Similar behavior was found when increasing the hydraulic diameter; the pressure drop increased by approximately up to 15 times between the smallest and the largest diameters. This is reflected in the real operation of a particulate filter due to the accumulation of soot inside the inlet cell that creates the cake layer on the porous medium and thus modifies the permeability. In addition to the change in permeability, the inlet section of the cell decreases, and the dimensionless pressure values increases accordingly.

The proposed model can be used to predict the backpressure determined by the particulate filter in the Internal Combustion Engine exhaust (ICE) systems. This is an important parameter that influences the ICE Efficiency, in fact, with the augmentation of the pressure drop the engine wastes more energy for the scavenging process. Here the regenerative process of the filter is able to restore the original working conditions, as to reduce the wasting work of expelling the fumes.

Finally, the formulation proposed in this study assumes the phenomena as stationary and isothermal process. Even if this assumption demonstrated to be capable to predict the trend of the particulate filter pressure drop against the main operating parameters, the numerical model can be potentially modified to account for the thermal gradients as well as time varying processes. These aspects may be hopefully investigated as future developments of the present study.

Appendix A

The mass balance for the input cell (cell 1) considering Darcy’s law for the filtration velocity and the ideal gas law for the density is



$$\frac{d}{dx}(p_1 u_1) = -\frac{4}{d} \frac{k}{\mu s} p_1 (p_1 - p_2) . \tag{A.1}$$

The dimensionless quantities are

$$\tilde{x} = \frac{x}{L}, \tilde{u}_i = \frac{u_i}{U} (i = 1,2), \tilde{p}_i = \frac{p_i - p_{atm}}{p} (i = 1,2), p^* = \frac{\mu U ds}{4Lk} . \tag{A.2}$$

Substituting Eqs. (A.2) into Eq. (A.1) and dividing by $U/(L p^*)$ the following result is obtained

$$\frac{d}{d\tilde{x}}(\tilde{p}_1 \tilde{u}_1) + \frac{p_{atm}}{p} \frac{d}{d\tilde{x}}(\tilde{u}_1) = -\frac{4}{d} \frac{k}{\mu s} \frac{L}{U} p^* \left(\tilde{p}_1 + \frac{p_{atm}}{p} \right) (\tilde{p}_1 - \tilde{p}_2) . \tag{A.3}$$

Defining $a=p_{atm}/p^*$ the following result is achieved

$$\frac{d}{d\tilde{x}}(\tilde{p}_1 \tilde{u}_1) + a \frac{d}{d\tilde{x}}(\tilde{u}_1) = -(\tilde{p}_1 + a)(\tilde{p}_1 - \tilde{p}_2) . \tag{A.4}$$

Following the same reasoning, for the output cell (cell 2) the dimensionless balance equation is

$$\frac{d}{d\tilde{x}}(\tilde{p}_2 \tilde{u}_2) + a \frac{d}{d\tilde{x}}(\tilde{u}_2) = (\tilde{p}_2 + a)(\tilde{p}_1 - \tilde{p}_2) . \tag{A.5}$$

Considering now the momentum balance equation for the input cell

$$\frac{1}{RT} \frac{d}{dx}(p_1 u_1^2) = -\frac{dp_1}{dx} - 2 f Re \frac{\mu}{d^2} u_1 , \tag{A.6}$$

and substituting Eqs. (A.2) into Eq. (A.9) and dividing by $U^2/(p^*RTL)$, the results is

$$\frac{d}{d\tilde{x}}(\tilde{p}_1 \tilde{u}_1^2) + \frac{p_{atm}}{p} \frac{d\tilde{u}_1^2}{d\tilde{x}} = -\frac{RT}{U^2} \frac{d\tilde{p}_1}{d\tilde{x}} - 2 f Re \frac{\mu}{d^2} U \frac{RTL}{U^2} \frac{1}{p} \tilde{u}_1 . \tag{A.7}$$

Defining $b=RT/U^2$ and $c=2 f Re \mu L U / (d^2 p_{atm})$ the following non-dimensional momentum balance equation is written

$$\frac{d}{d\tilde{x}}(\tilde{p}_1 \tilde{u}_1^2) + a \frac{d\tilde{u}_1^2}{d\tilde{x}} = -b \frac{d\tilde{p}_1}{d\tilde{x}} - a b c \tilde{u}_1 . \tag{A.8}$$

Following the same reasoning, for the output cell (cell 2) the dimensionless momentum equation is

$$\frac{d}{d\tilde{x}}(\tilde{p}_2 \tilde{u}_2^2) + a \frac{d\tilde{u}_2^2}{d\tilde{x}} = -b \frac{d\tilde{p}_2}{d\tilde{x}} - a b c \tilde{u}_2 . \tag{A.9}$$

Appendix B

The filtration velocity v_f is defined through Darcy's law

$$p_1 - p_2 = \frac{\mu}{k} s v_f . \tag{B.1}$$

Substituting the dimensionless quantities

$$\tilde{v}_f = \frac{4L}{dU} v_f , \tilde{p}_i = \frac{p_i - p_{atm}}{p} (i = 1,2), p^* = \frac{\mu U ds}{4Lk} , \tag{B.2}$$

inside Eq. (B.1), and simplifying and considering the parameter p^* defined in eq. (B.2), the result is

$$\tilde{p}_1 - \tilde{p}_2 = \tilde{v}_f . \tag{B.3}$$

Author Contributions

L. Montorsi and M. Milani devised the scheme and started the project. A.N. Impiombato developed the mathematical and numerical modeling, examined the validation of the theory and obtained all the results. C. Biserni contributed to the drafting of the manuscript in providing it with the necessary elegance. The manuscript was written through the contribution of all authors. All authors discussed the results, reviewed, and approved the final version of the manuscript.

Acknowledgments

Not applicable.



Conflict of Interest

The authors declared no potential conflicts of interest with respect to the research, authorship, and publication of this article.

Funding

The authors received no financial support for the research, authorship, and publication of this article.

Data Availability Statements

The datasets generated and/or analyzed during the current study are available from the corresponding author on reasonable request.

Nomenclature

a, b, c	Dimensionless parameters	U	Inlet cell velocity, [m s ⁻¹]
Abstol	Absolute tolerance	u	Fluid velocity, [m s ⁻¹]
d	Hydraulic diameter/cell dimension, [m]	Vf	Filtration velocity through the porous wall, [m s ⁻¹]
f	Friction factor	x	Cartesian coordinate, [m]
k	Porous medium permeability, [m ²]	ε	Percentual discrepancy error
L	Monolith length, [m]	ρ	Fluid density, [kg m ⁻³]
p	Pressure, [Pa]	μ	Dynamic viscosity, [kg m ⁻¹ s ⁻¹]
Re	Reynolds number	(~)	Dimensionless variables
RelTol	Relative tolerance	(*)	Dimensionless variables
res	Residual	1	Inlet cell
s	Porous media wall thicknesses, [m]	2	Outlet cell
R	ideal gas constant for air, [J kg ⁻¹ K ⁻¹]	atm	Atmospheric
S(x)	Computed solution	ref	Reference
T	Temperature, [K]		


References


- [1] Niessner, R., The many faces of soot: characterization of soot nanoparticles produced by engines, *Angewandte Chemie International Edition*, 53(46), 2014, 12366-79.
- [2] Tollefson, J., Soot a major contributor to climate change, *Nature News*, 2013.
- [3] Torregrosa, A. J., Serrano, Serrano, J. R., Arnau, F. J., and Piqueras, P., A fluid dynamic model for unsteady compressible flow in wall-flow diesel particulate filters, *Energy*, 36(1), 2011, 671-84.
- [4] Fragassa, C., Electric city buses with modular platform: a design proposition for sustainable mobility, In: *Campana G. et al. (eds) Sustainable Design and Manufacturing 2017. SDM 2017. Smart Innovation, Systems and Technologies*, vol. 68. Springer, Cham, Switzerland, 2017.
- [5] Minak, G., Fragassa, C., Vannucchi de Camargo, F., A Brief Review on Determinant Aspects in Energy Efficient Solar Car Design and Manufacturing, In: *Campana G. et al. (eds) Sustainable Design and Manufacturing 2017. SDM 2017. Smart Innovation, Systems and Technologies*, vol. 68. Springer, Cham, Switzerland, No. 14.6, 2017.
- [6] Minak, G., Brugo, T., Fragassa, C., Pavlovic, A., Zavatta, N., De Camargo, F., Structural Design and Manufacturing of a Cruiser Class Solar Vehicle, *Journal of Visualized Experiments*, 143, 2019, e58525
- [7] Prantoni, M., Aleksandrova, S., Medina, H., Saul, J., Benjamin S., and Afonso, O.G., Modelling pressure losses in gasoline particulate filters in high flow regimes and temperatures, *SAE Technical Paper Series*, 2019, 2019, .
- [8] Bissett, E.J., Mathematical model of the thermal regeneration of a wall-flow monolith diesel particulate filter, *Chemical Engineering Science*, 39(7-8), 1984, 1233-44.
- [9] Prantoni, M., Aleksandrova, S., Medina H., and Benjamin, S., Multi-channel modelling approach for particulate filters, *Results in Engineering*, 5, 2020, 100077.
- [10] Aleksandrova, S., Saul, J., Prantoni, Medina, H., Garcia-Afonso, O., Bevan, M., and Benjamin, S., Turbulent flow pressure losses in gasoline particulate filters, *SAE International Journal of Engines*, 12(4), 2019, 455-70.
- [11] Koltzakis, G., Haralampous, O., Depcik C., and Ragone, J.C., Catalyzed diesel particulate filter modeling, *De Gruyter*, 2013.
- [12] Yang, S., Deng, C., Gao, Y., and He, y., Diesel particulate filter design simulation: A review, *Advances in Mechanical Engineering*, 8(3), 2016, 1-14.
- [13] Rettinger, C., Rude, U., A coupled lattice Boltzmann method and discrete element method for discrete particle simulations of particulate flows, *Computers & Fluids*, 172, 2018, 706-719.
- [14] Wang, L.P., Peng, C., Guo, Z., e Yu, Z., Lattice Boltzmann simulation of particle-laden turbulent channel flow, *Computers & Fluids*, 124, 2016, 226-36.
- [15] Lantermann, U., Hanel, D., Particle Monte Carlo and lattice-Boltzmann methods for simulations of gas-particle flows, *Computers & Fluids*, 36(2), 2007, 407-22.
- [16] Huang, J., Xiao, F., Dong, H., e Yin, X., Diffusion tortuosity in complex porous media from pore-scale numerical simulations, *Computers & Fluids*, 183, 2019, 66-74.
- [17] Wei, H., Chen, J.S., Hillman, M., A stabilized nodally integrated meshfree formulation for fully coupled hydro-mechanical analysis of fluid-saturated porous media, *Computers & Fluids*, 141, 2016, 105-15.
- [18] Gervais, P.C., Bourrous, S., Dany, F., Bouilloux, L., Ricciardi, L., Simulations of filter media performances from microtomography-based computational domain. Experimental and analytical comparison, *Computers & Fluids*, 116, 2015, 118-28.
- [19] Celli, M., Impiombato, A.N., Barletta, A., Buoyancy-driven convection in a horizontal porous layer saturated by a power-law fluid: The effect of an open boundary, *International Journal of Thermal Sciences*, 152, 2020, 106302.
- [20] Tilton, N., Serre, E., Martinand, D., Lueptow, R.M., A 3D pseudospectral algorithm for fluid flows with permeable walls. Application to filtration, *Computers & Fluids*, 93, 2014, 129-45.
- [21] Yu, K.G., Yang, Z.H., Assembly variation modeling method research of compliant automobile body sheet metal parts using the finite element method, *International Journal of Automotive Technology*, 16(1), 2015, 51-6.
- [22] Chen, X.-W., Zhou, Y., Modelling and Analysis of Automobile Vibration System Based on Fuzzy Theory under Different Road Excitation Information, *Complexity*, 2018.
- [23] Kim, D.H., Kim, H.G., Kim, H.S., Design optimization and manufacture of hybrid glass/carbon fiber reinforced composite bumper beam for automobile vehicle, *Composite Structures*, 131, 2015, 742-752.
- [24] Pavlovic, A., Fragassa, C., Geometry optimization by fem simulation of the automatic changing gear, *Reports in Mechanical Engineering*, 1, 2020, 199-205.
- [25] Shatrov, M.G., Dunin, A.U., Dushkin, P.V., Yakovenko, A.L., Golubkov, L.N., Sinyavski, V.V., Influence of pressure oscillations in common rail injector on fuel injection rate, *Facta Universitatis-Series Mechanical Engineering*, 18(4), 2020, 579-593.
- [26] Sinyavski, V., Shatrov, M., Kremnev, V., Pronchenko, G., Forecasting of a boosted locomotive gas diesel engine parameters with one- and two-stage charging systems, *Reports in Mechanical Engineering*, 1(1), 2020, 192-198.





- [27] Kirubagharan, R., Ramesh, C., Pragalathan, P., Harish, N., Geometrical analysis of automobile radiator using CFD, *Materials Today: Proceedings*, 33, 2020, 3124-3130.
- [28] Mohamad, B., Karoly, J., Zelentsov, A., CFD modelling of formula student car intake system, *Facta Universitatis-Series Mechanical Engineering*, 18(1), 2020, 153-63.
- [29] Martins, L.R., Guimaraes, G.P., Fragassa, C., Acoustical performance of Helmholtz resonators used as vehicular silencers, *FME Transactions*, 46(4), 2018, 497-502.
- [30] Cooper, J., Liu, L., Ramskill, N., Watling, T., York, A., Stitt, E., Sederman A., Gladden, L., Numerical and experimental studies of gas flow in a particulate filter, *Chemical Engineering Science*, 209, 2019, 115179.
- [31] MATLAB, 9.7.0.1190202 (R2020b), Natick, Massachusetts: The MathWorks Inc., 2020.
- [32] Konstandopoulos, A.G., Johnson, J.H., Wall-flow diesel particulate filters-their pressure drop and collection efficiency, *SAE Transactions*, 1989.
- [33] Laugier A., Garai, J., Derivation of the ideal gas law, *Journal of Chemical Education*, 84(11), 2007, 1832.
- [34] Sutherland, W., LII. The viscosity of gases and molecular force, *The London, Edinburgh, and Dublin Philosophical Magazine and Journal of Science*, 36(223), 1893.
- [35] Rosner, D.E., Transport processes in chemically reacting flow systems, *Courier Corporation*, 2012.
- [36] Kierzenka, J., Shampine, L.F., A BVP solver that controls residual and error, *Journal of Numerical Analysis, Industrial and Applied Mathematics*, 3, 2008, 27-41.
- [37] Koga, T., Introduction to kinetic theory stochastic processes in gaseous systems; London: Pergamon Press Oxford, 1970.

ORCID iD

Andrea Natale Impiombato  <https://orcid.org/0000-0003-1103-8058>

Cesare Biserni  <https://orcid.org/0000-0003-0081-2036>

Massimo Milani  <https://orcid.org/0000-0001-6257-6919>

Luca Montorsi  <https://orcid.org/0000-0002-4910-5693>



© 2022 Shahid Chamran University of Ahvaz, Ahvaz, Iran. This article is an open access article distributed under the terms and conditions of the Creative Commons Attribution-NonCommercial 4.0 International (CC BY-NC 4.0 license) (<http://creativecommons.org/licenses/by-nc/4.0/>).

How to cite this article: Impiombato A.N., Biserni C., Milani M., Montorsi L. Prediction Capabilities of a One-Dimensional Wall-Flow Particulate Filter Model, *J. Appl. Comput. Mech.*, 8(1), 2022, 245-259. <https://doi.org/10.22055/JACM.2021.38708.3270>

Publisher's Note Shahid Chamran University of Ahvaz remains neutral with regard to jurisdictional claims in published maps and institutional affiliations.

